

INITIAL DEVELOPMENT OF A CFD ICING TOOL

Jayme R. Teixeira da Silva¹, Maria E. M. C. Lopes¹, Augusto P. R. Preguiça¹, Caio F. Rafael¹, Pedro C. de Souza Villela¹, Guilherme A. Lima da Silva² & Hrvoje Jasak^{3,4}

¹ATS Aerothermal Solutions, Sao Paulo, SP, Brazil
²Aerothermal Solutions and Software Distributor LLC, Miami, FL, USA
³The Cavendish Laboratory, Department of Physics, University of Cambridge, Cambridge, UK
⁴Wikki Ltd., London, UK

Abstract

This paper presents the initial development of a three-dimensional ice accretion tool based on Foam-extend 5.0, a Computational Fluid Dynamics (CFD) suite. The final tool will include Foam-extend features, such as the finite area water model, the immersed boundary, laminar-turbulent transition, solid wall conduction, and turbulent rough convective heat transfer, along with some specifically designed extensions, solvers, and functions to perform ice shape and protection simulations. The proposed tool is a unified CFD solution capable of modeling the entire process in 3D. In this article, the authors introduce a new tool called iceAccretionFoam. This tool represents the initial phase toward a final tool and it uses Foam-extend's immersed boundary and Eulerian droplet trajectories to simulate impingement and the growth of rime ice. The tool evaluates and verifies the accuracy of linear solvers for pressure, turbulence, and TVD schemes by employing the NACA0012 airfoil. It simulates rime icing conditions with accretion alone, without considering thermodynamics. The simulation considers parameters such as median volumetric diameter, liquid water content, airspeed, free-stream temperature, three models of ice density, and different droplet distributions.

Keywords: aircraft icing, eulerian dispersed phase, rime ice, impingement, ice growth

1. Introduction

Regarding three-dimensional icing codes, NASA's LEWICE3D [1] is a pioneering code dealing with icing in 3D. This code uses the flow solution from external CFD and calculates the droplet trajectories using the Lagrangian formulation. Although the flow solutions and impingement are three-dimensional, the mathematical model for the water film adopts a two-dimensional approach, considering normal slices over a leading edge of the wing. Similarly to the water model, the thermodynamics and growth of ice are also calculated within two-dimensional slices. This approach is called a quasi-3D solution to the ice-accretion problem. Instead of following the shear lines, the code makes several cuts to the wing in the normal direction to the leading edge. Depending on the degree of angle of sweep, the shear lines form an accentuated curve after stagnation and depart significantly from the normal direction cut made by LEWICE3D [1].

The FENSAP code [2], originally developed by the Habashi team at McGill University, uses a 3D CFD flow solution and calculates droplet trajectories using a Eulerian formulation. In addition to the impingement module, the FENSAP code also includes modules for heat transfer and ice growth. These three droplet modules, along with the CFD flow equations, are interactively solved to calculate the final shape of the ice.

Regarding acceptance by authorities, no 3D code is widely accepted, despite 2D codes being recognized and accepted for specific applications, mainly on wings. This weak acceptance is due to the fact that the technology for 3D ice accretion has not yet been entirely developed. For example, no code accurately reproduces the formation of the glaze ice lobster tail in the swept wings.

2. Objective

The purpose of this document is to present the initial development of a novel three-dimensional (3D) ice accretion simulation utilizing Foam-extend 5.0. Furthermore, the validation process encompasses an assessment of classical rime ice in the NACA0012 airfoil profile, as established by Shin and Bond [3], augmented by assessments using traditional airfoil data from NACA0012 for C_p [4] and numerical results from NACA0012 LEWICE for β [5], in light of the lack of experimental data β relevant to this particular airfoil configuration.

3. Ice Accretion Tool Description

The Foam-extend 5.0 numerical simulation library is a fork of the original foam code [6] developed by Jasak and Weller at Imperial College in the 1990s [7, 8]. The authors of the present paper are developing a new tool named iceAccretionFoam, which includes the standard foam extension features, such as the finite-area water model and the immersed boundary.

A single 3D CFD code is all that is needed for all calculations. This initial tool is only suitable for the rime ice regime; however, the framework is designed to include all the components necessary for the development of mixed and glaze ice. In this case, the task will involve integrating convective heat transfer [9, 10] along with transition [11, 12], the solidification process, and the dynamics of water at the interface by applying the finite area technique [13] adapting previous experience [14].

3.1 Solver Charactheristics

The iceAccretionFoam solver for rime icing accretion, as delineated in this manuscript, exhibits distinctive attributes.

- 1. A transient solution of the flow by using Reynolds Averaged Navier-Stokes incompressible equations in a Δt_{flow} and growing ice in a larger $\Delta t_{accretion}$, simulating it as multi-step with Unsteady Reynolds Averaged Navier-Stokes (URANS);
- 2. An immersed boundary method [15] that updates the frontier of the solid surface and defines the mesh around the new surface created by the growth of the ice;
- 3. A capability to receive a user-defined droplet distribution [16, 17] with *n* bins based on the median volumetric diameter (MVD) and fraction of the freestream liquid water content (FLWC);
- 4. An implementation of the Langmuir-D-type distribution [18] incorporating a 7-bin diameter and freestream liquid water content (FLWC), contingent upon the provision of a median volumetric diameter (MVD) by the user;
- 5. An Eulerian-dispersed phase model adapted from the extant driftEulerFoam solver. Each droplet diameter is treated as a distinct phase, characterized by the volumetric water fraction, α , and the phase velocity, U_{phase} .

3.2 Simplifying Assumptions

To ensure that the problem aligns with the rime ice shape simulation for the current analysis, the following assumptions are made: a) All impinging water instantaneously solidifies upon contact; b) A normal growth of ice rule is applied to all surfaces subjected to impingement; c) Thermal balance and convective heat and mass transfer computations are not considered; d) Liquid water is assumed not to exist on the surface of the airfoil; e) The airfoil surface is assumed to be adiabatic; f) Thermal conduction within the airfoil surface is neglected; g) Phenomena such as splashing, re-impingement, and other secondary effects associated with Super Large Droplets (SLD) are disregarded; h) The droplet is modeled as a perfect sphere, and the drag correlation omits deformation effects; i) The droplet weight is not considered. These assumptions will change according to the iceAccretionFoam code evolution, for example, when simulating glaze ice shape, SLD or thermal ice protection system in future versions.

3.3 Numerical Mesh for Ice Growth

Numerical modeling in ice accretion simulations must account for substantial changes in the geometry of the flow domain due to ice accretion on solid walls. To handle this, the Immersed Boundary Surface Method [15] is applied, where the body-fitted fixed polyhedral background mesh is modified using a deforming immersed triangular surface. The interaction between the immersed surface and the background mesh is developed in the spirit of immersed boundary solvers.

4. Mathematical Models

4.1 Main Air Flow

The PIMPLE algorithm is used in computational fluid dynamics for transient simulations. It merges the SIMPLE algorithm [19] with the PISO algorithm [20]. This method is designed for efficient solutions in fluid flow problems, especially in cases with unsteady flows, large time steps, or significant coupling between velocity and pressure. The equations for the primary airflow are provided in the following [21].

$$\frac{\partial \mathbf{U}}{\partial t} + \nabla \cdot (\mathbf{U}\mathbf{U}) - \nu \nabla^2 \mathbf{U} = -\nabla p \tag{1}$$

$$\nabla^2 p = \nabla \cdot \mathbf{H}(\mathbf{U})$$
 where $\mathbf{H}(\mathbf{U}) = -\nabla \cdot (\mathbf{U}\mathbf{U})$ (2)

4.2 Dispersed Phase Flow

The iceAccretionFoam utilizes drift flux modeling to simulate separate phases as a single mixture phase. The incompressible dispersed phase, represented by U_{phase} and α , is determined using the driftFlux model. Each droplet diameter in the distribution is treated as an individual phase.

$$\left\| \vec{U}_{rel} \right\| = \left\| \vec{U}_{phase} - \vec{U} \right\| \tag{3}$$

$$Re_{rel} = max(2.4, \left\| \vec{U}_{rel} \right\| \cdot \frac{d}{v_D})$$
 (4)

$$C_d = max \left[0.5, \frac{24}{Re_{rel}} (1 + 0.15 \cdot Re_{rel}^{0.687}) \right]$$
 (5)

$$DragPf = \frac{3}{4} \cdot Cd \cdot \frac{\rho_C}{\rho_D} \cdot \frac{\left\| \vec{U}_{rel} \right\|}{d}$$
 (6)

The equation for U_{phase} , droplet phase velocity, is defined as follows:

$$\frac{\partial \tilde{\mathbf{U}}_{\mathbf{phase}}}{\partial t} + \nabla \cdot (\vec{\phi}_{cont} \cdot \tilde{\mathbf{U}}_{\mathbf{phase}}) =
\mathbf{g} + DragPf(\tilde{\mathbf{U}}_{\mathbf{rel}}) - \frac{3}{4}C_d \cdot ||\vec{U}_{rel}|| \cdot v_t \cdot \frac{\nabla \alpha}{d}$$
(7)

Where ϕ_{cont} is the flux of the continuous phase or the main flow. The equation for α , volumetric fraction, is listed below:

$$\frac{\partial \alpha}{\partial t} + \nabla \cdot (\tilde{\phi}_{\mathbf{phase}} \cdot \alpha) = 0 \tag{8}$$

Here ϕ_{phase} is the flux of the droplet phase or the flow of the dispersed phase.

4.3 Ice Growth Modeling

From the equations 9 and 10, one can calculate the height of the ice, h_{ice} , on the surface subjected to the impingement of water droplets based on the cumulative height parcel of each phase i:

$$h_{ice,i} = \Delta t_{accretion} \cdot \alpha_i \cdot U_{phase,i} \cdot \frac{\rho_{water}}{\rho_{ice}}$$
(9)

$$h_{ice} = \sum_{i=1}^{n} h_{ice,i} \tag{10}$$

The deformed field, which represents the height of the ice (h_{ice}) , is used to modify the computational domain of the immersed boundary. A minimum threshold for boundary movement is established to determine when the boundary should be updated. The height is used to move the boundary normally to the surface at each point of the mesh.

The process of ice growth can be fully simulated in a transient manner, which means that ice accretion occurs at each time step of the flow solution. Alternatively, to simulate the ice formation process, the time interval for the flow solution (Δt_{flow}) can be shorter than the time interval for ice accretion $(\Delta t_{accretion})$. Thus, the total time for accretion can be divided into $nt = t_{total}/\Delta t_{accretion}$ steps, with a flow solution of Δt_{flow} between each step. The user can arbitrarily choose the values of Δt_{flow} and $\Delta t_{accretion}$ to maintain accuracy while simultaneously accelerating the solution. In this multistep solution condition for ice growth, it is assumed that the collection efficiency remains relatively constant for the defined time interval $\Delta t_{accretion}$.

4.4 Ice Density

This study investigated three ice density models: LEWICE [22]; Jones [23]; and Macklin [24]. The density of ice is influenced by the quantity of air trapped during its formation and therefore depends on factors such as the median volumetric diameter, liquid water content, size of the body, freestream velocity, and recovery temperature of the surface. The density of ice is reduced by trapped air, as seen in glaze ice, whereas the density of ice is increased by a more compact or rime-like formation. For LEWICE [22]:

$$\rho_{ice} = 1000 \cdot \exp\left[0.15 \cdot (1 + 6043 \cdot S^{-2.65})\right] \tag{11}$$

$$\rho_{ice} = 1000 \cdot \exp\left[0.15 \cdot (1 + 6043 \cdot S^{-2.65})\right]$$

$$S = \frac{\mathsf{MVD}^{0.82} \cdot U_{\infty}^{0.59} \cdot \mathsf{LWC}^{0.21}}{d_{le}^{0.48} \cdot (-T_{rec}^{0.23})}$$
(11)

For Jones [23]:

$$\rho_{ice} = 0.210 \cdot R^{0.53} \qquad R \le 10
\rho_{ice} = \frac{R}{1.15 \cdot R + 2.94} \qquad 10 < R < 60
\rho_{ice} = 0.84 \qquad R \ge 60$$
(13)

where R is the Macklin parameter $-d_{le} \times U_{\infty}/(2T_{rec})$, where d_{le} is the diameter of the leading edge, U_{∞} is the freestream velocity, T_{rec} is in Celsius, thus, a negative value and lower than zero. For Macklin [24]:

$$\rho_{ice} = 0.110 \cdot R^{0.76} \quad R \le 17 \\
\rho_{ice} = 0.9 \quad R > 17$$
(14)

The only local parameter considered is the recovery temperature T_{rec} , which varies along the surface and depends on the local Mach number (M) that depends on the local pressure values.

$$T_{\mathsf{rec}} = T_{\infty} \cdot \left(1 + r \cdot \frac{\gamma - 1}{2} \cdot M_{\mathsf{local}}^2 \right)$$
 (15)

$$T_{\text{rec}} = T_{\infty} \cdot \left(1 + r \cdot \frac{\gamma - 1}{2} \cdot M_{\text{local}}^{2} \right)$$

$$M_{\text{local}} = \sqrt{\frac{2}{\gamma - 1} \left[\left(\frac{P_{\text{local}}}{P_{total,\infty}} \right)^{-\frac{\gamma - 1}{\gamma}} - 1 \right]}$$
(15)

where $r = Pr^{1/3}$ for turbulent flows and $\gamma = 1.4$ for air. If the solver had compressibility capability and solved the energy equation, the simulation would yield the value of T_{rec} due to the effects of compression and kinetic heating caused by viscosity. In the current model, the flow equations are assumed to be incompressible, and the energy equation is not solved, therefore, the Eq. (15) is required. This is only an initial approach to allow for the calculation of the density of the ice.

5. Test Cases

5.1 Droplet Distributions

Three different distributions were used in this study: a) the distribution used by Papadakis [17] in various studies carried out at NASA IRT, as shown in Table 1; b) the distribution utilized by Wright [16] to validate the LEWICE 3.0 software, detailed in Table 2; and c) the theoretical distribution of Langmuir-D, a widely cited distribution recognized by authorities [25, 18], as illustrated in Table 3.

Table 1 – Discrete Cumulative Distribution of Papadakis [17] with MVD = 20 μm

Cumulative % LWC	% LWC	D(I) / MVD	D(I)
97.5	5	0.2770	5.540
90.0	10	0.4460	8.920
75.0	20	0.6817	13.634
50.0	30	1.0000	20.000
25.0	20	1.5865	31.730
10.0	10	2.2943	45.886
2.5	5	3.2542	65.084

Table 2 – Distribution of Wright [16] with MVD = 21 μm

%LWC	D(I)
0.1390	8.6
0.0958	12.5
0.0997	15.5
0.1220	18.5
0.1208	21.5
0.1115	24.5
0.0917	27.5
0.0946	31.6
0.0899	48.2
0.0350	95.9

5.2 Pressure Coefficient C_p

The pressure coefficient is computed along the surface by:

$$C_p = \frac{p - p_{\infty}}{\frac{1}{2}\rho U_{\infty}^2},\tag{17}$$

where p and p_{∞} represent the pressure values in the local and far fields, respectively. Furthermore, p denotes the density and U_{∞} represents the velocity in the far field. The experimental data of C_p were obtained from Emmons' NACA investigation [4] carried out under conditions of incompressibility, specifically at Mach zero and angle of attack (AOA) of 0° . In addition, the XFoil solver [26] was used to compare the results for an AOA of zero. Reynolds and Mach numbers were determined on the basis of free-stream conditions, and the transition from laminar to turbulent flow took place immediately after the stagnation point. This ensures that the results C_p are fully turbulent and account for the viscosity.

Table 3 – Theoretical L	_angmuir-D Distribution	[18] with MVD = 20 μm

%LWC	(a/ao) ²	D(I)
5	0.31	6.2
10	0.52	10.4
20	0.71	14.2
30	1.00	20.0
20	1.37	27.4
10	1.74	34.8
5	2.22	44.4

5.3 Collection Efficiency β

Due to the lack of experimental data on the airfoil collection efficiency of NACA0012, this study used LEWICE-simulated results, as compiled by Al-Khalil (2001) [5]. The scenarios include a NACA0012 with a 0.9144 m chord, an AOA of 0° , an incoming flow velocity U_{∞} , of 100 mph, a liquid water content, LWC, of 0.55 g/m^3 , and a median volumetric diameter, MVD, of 20 μm . The collection efficiencies, β_i and β_{tot} , can be defined as follows:

$$\beta_i = \frac{\alpha_i \cdot \vec{U}_{phase,i} \cdot \vec{n}}{\alpha_{\infty} \cdot |\vec{U}_{phase,\infty}|} \tag{18}$$

$$\beta_{tot} = \sum_{i=1}^{n} \frac{\alpha_i \cdot \beta_i}{\alpha_{\infty}} \tag{19}$$

$$\alpha_{\infty} = \sum_{i=1}^{n} \alpha_{i} \tag{20}$$

where i is the phase and n is the number of phases. The values of α_{∞} and each α_i are defined in Tables 1, 2 and 3. The β_{tot} is determined by weighting the values of β_i by α_i , as shown in Eq. 20.

5.4 Rime Ice

Shin and Bond [3, 27] investigated cases of rime formation at a static temperature (T_{∞}) of -15 °F, with an MVD of 20 μ m, LWC of 1.0 g/m^3 and U_{∞} of 150 mph. They conducted their experiments using a NACA0012 airfoil with a 0.53 m chord and measured the accretion shape at 360 s duration for this specific case. The authors of this study adopted the test section at a pressure altitude of 2,000 feet.

6. Simulation Configuration

6.1 Linear Solver for Pressure

The Preconditioned Conjugate Gradient (PCG) method is frequently preferred for its efficiency in solving symmetric positive definite matrices, making it suitable for aerodynamic simulations with extensive and sparse matrix systems [28]. However, in highly complex scenarios, its accuracy may be slightly compromised. On the other hand, the Algebraic Multigrid (AMG) solver is acclaimed for its robustness and scalability, making it highly suitable for addressing intricate aerodynamic challenges with fluctuating coefficients. Provides an optimal balance between velocity and precision [29]. The

Geometric Algebraic Multigrid (GAMG) solver combines the strengths of geometric and algebraic methodologies, delivering elevated accuracy for expansive aerodynamic projects. However, it might incur higher computational costs compared to PCG [30].

The consistent results from the GAMG, AMG and PCG solvers for C_p and impingement β over the airfoil are likely due to the simplicity of the flow conditions, since there is no recirculation, complex geometry, or separation bubbles. These solvers converge to the same solution because the problem is straightforward and well-posed, ensuring that the underlying physics is accurately captured without significant numerical challenges. However, this condition may change if the ice shape is large and nonuniform, as in the case of glaze ice.

6.2 TVD Schemes

Management of discontinuities within the water concentration field, α , represents an important element in aerodynamic simulations, especially when employing TVD (Total Variation Diminishing) schemes. The LUST (Limited Upwind Scheme for Transport) has been shown to be instrumental in reducing numerical diffusion, a critical factor for the precise delineation of shadow zones and for the prevention of synthetic concentration peaks at stagnation points. By blending first-order and second-order schemes, LUST effectively balances accuracy and stability in aerodynamic simulations [31]. The MUSCL (Monotonic Upstream-Centered Scheme for Conservation Laws) enhances the Godunov scheme to achieve superior resolution of steep gradients, thereby preserving the integrity of discontinuities in α while preventing the occurrence of false oscillations [32]. Performing well in the management of flow discontinuities, the Van Leer scheme demonstrates particular proficiency in regulating variations of the concentration field near stagnation points [33]. The MINMOD limiter (Minimum Modulus) preserves monotonicity and effectively prevents the formation of nonphysical concentration peaks in complex flow domains [34]. Furthermore, the Second-Order Upwind Scheme, by assimilating downstream information, improves the accuracy in depicting α across discontinuities, which proves advantageous for the prediction of concentration fields in aerodynamic flows [35]. The current simulation, which reveals shadow zones with zero water concentration followed by a peak

The current simulation, which reveals shadow zones with zero water concentration followed by a peak and subsequent decay to freestream values, demonstrates that the Second-Order Upwind scheme has demonstrated accuracy and convergence stability. On the other hand, LUST is more accurate for the peak of water impingement but less stable than the Second-Order Upwind scheme.

6.3 Turbulence Models

The $k-\varepsilon$ realizable model provides improvements, especially in predicting the spread rate of jets and flows that involve rotation and boundary layers under strong adverse pressure gradients, making it more suitable for complex aerodynamic applications [36]. The $k-\omega$ SST model is highly respected in aerodynamics, particularly for its ability to accurately capture the effects of the boundary layer due to its formulation, which blends the behavior of $k-\omega$ in the region near the wall with $k-\varepsilon$ in the far field [37]. The Spalart-Almaras turbulence model [38] is a one-equation model specifically designed for aerospace applications. It excels in wall-bounded flows and adverse pressure gradient scenarios. Being a low Reynolds number model, it does not utilize wall functions, making it suitable for near-wall turbulence.

In contrast, the $k-\varepsilon$ model, known for its straightforwardness and efficiency, is typically effective for fully turbulent flows but may lack precision in the near-wall region, making it less suitable for detailed boundary layer predictions [39]. However, in this particular simulation, the $k-\varepsilon$ model performs adequately since it does not necessitate a boundary layer or near-wall viscous calculation, given that it is a Eulerian impingement that can be executed with a non-viscous flow solution. As a result, all turbulence models yield very similar outcomes in this scenario. Thus, the $k-\varepsilon$ model was selected for its simplicity and quicker computational time.

In the context of glaze ice accretion, convective heat transfer and skin friction are crucial. The accuracy of turbulence models in the near-wall region is critical as it directly impacts the formation of glaze ice, which forms when supercooled water droplets freeze after impact in the runback water, heavily influenced by heat transfer rates. However, rime ice accretion involves a dry growth of ice without thermal balance, forming instantly as supercooled droplets impact the aircraft at colder temperatures.

Thus, the precision of turbulence models in the near-wall region is not as critical for rime ice accretion as it is for glaze ice accretion.

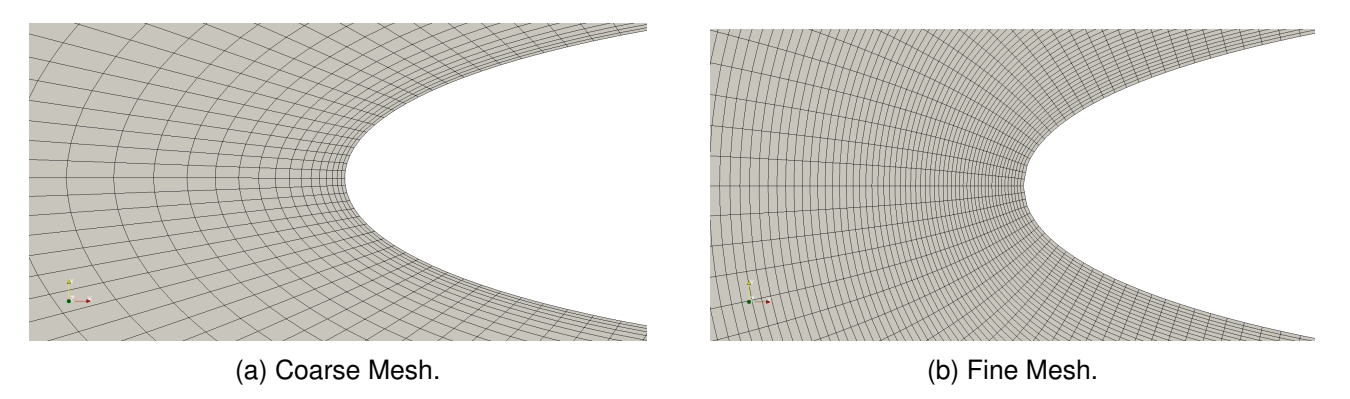


Figure 1 – Meshes used for β and C_p simulations

6.4 Numerical Meshes

The mesh used in this study is composed of O-Type, structured, and hexahedral elements, notably excluding any prism layers. The coarse mesh consists of approximately 7,000 elements, with the leading edge shown in Figure 1a, while the fine mesh comprises around 66,000 elements, as shown in Figure 1b. The absence of prism layers is intentional, as simulation of impingement and rime ice accretion does not necessitate a highly accurate viscous-flow solution for heat transfer or friction. Consequently, a simplified flow solution, such as the potential flow or Euler equations, is sufficient to resolve the flow characteristics without significant issues. However, the fine mesh is essential for offering higher resolution to the ice-growth formation because the current authors are using an immersed boundary method approach.

6.5 Boundary Conditions

Pressure p is the zero-gradient freestream type along all external boundaries, while velocity U is the freestream type with a fixed value. The velocity U_{phase} at the boundaries is equal to U, and there is a zero gradient for the incoming particles and a fixed zero value for the outgoing particles at the faces. The setup of α is similar to U_{phase} for the surface and is given by LWC in the freestream by using the relation:

$$\alpha_{\infty} = \frac{LWC_{\infty}}{\rho_{water}} \tag{21}$$

7. Numerical Results

The authors present three types of results: pressure coefficient, collection efficiency, and rime ice shape. The accuracy of the predicted rime ice shape is strongly influenced by the efficiency of droplet collection as well as the distribution of water concentration. Furthermore, the collection efficiency is directly dependent on the pressure coefficient and the velocities normal to the airfoil surface. This dependency is why this paper not only presents the rime ice shapes but also includes the results of C_p and β as part of a validation process for the NACA0012 airfoil.

7.1 Pressure Coefficient - C_p

Figure 2 illustrates the negative pressure coefficient $(-C_p)$ along the chord length of a NACA0012 airfoil at a zero-degree AOA. The results of the present study are compared with the Emmons experimental data [4] and the Xfoil [26] results, obtained through simulations under incompressible flow conditions with M = 0.2 and Re = 4.6E6. The full turbulent simulation in Xfoil is ensured by fixing the transition immediately after the stagnation point.

Despite the fact that XFoil uses a Kármán-Tsien [40] correction for C_p , the current authors employed the Prandtl-Glauert [41] transformation in conjunction with the GAMG, AMG and PCG solvers as

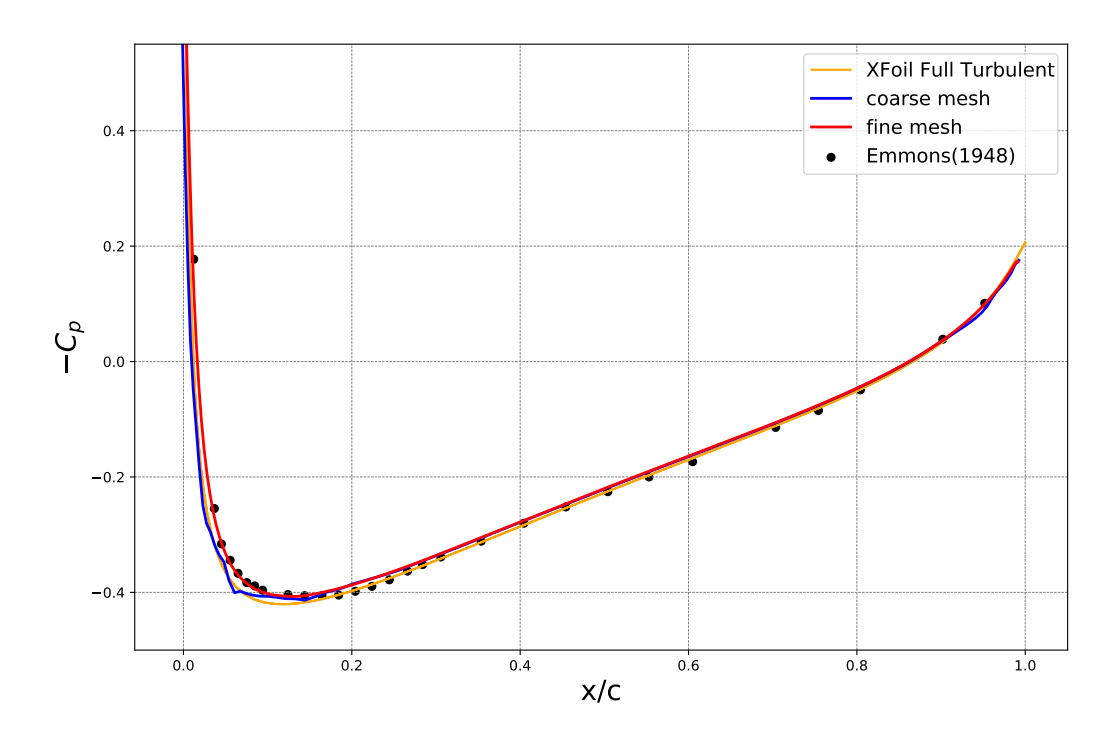


Figure 2 – C_p distributions at 0° AOA. AMG Solver. $K - \varepsilon$ Turbulence Model.

delineated below. This would not affect the correction since the Mach number is outside the compressible and far from the transonic regime.

$$C_p^* = C_p \cdot \frac{1}{\sqrt{1 - M_\infty^2}} \tag{22}$$

where M_{∞} is the Mach number in the freestream. This correction helps the computational results to be close to Emmons' experimental data [4], particularly evident in the low-pressure peak near the leading edge, which is the region most important for ice formation.

Upon comparing the coarse mesh with the fine mesh, it becomes evident that the fine mesh exhibits a closer adherence to experimental data compared to both XFoil and the coarse mesh. Furthermore, the fine mesh yields a smoother solution, devoid of discontinuities, in contrast to the coarse mesh. This difference will lead to different impingement results for coarse and fine meshes.

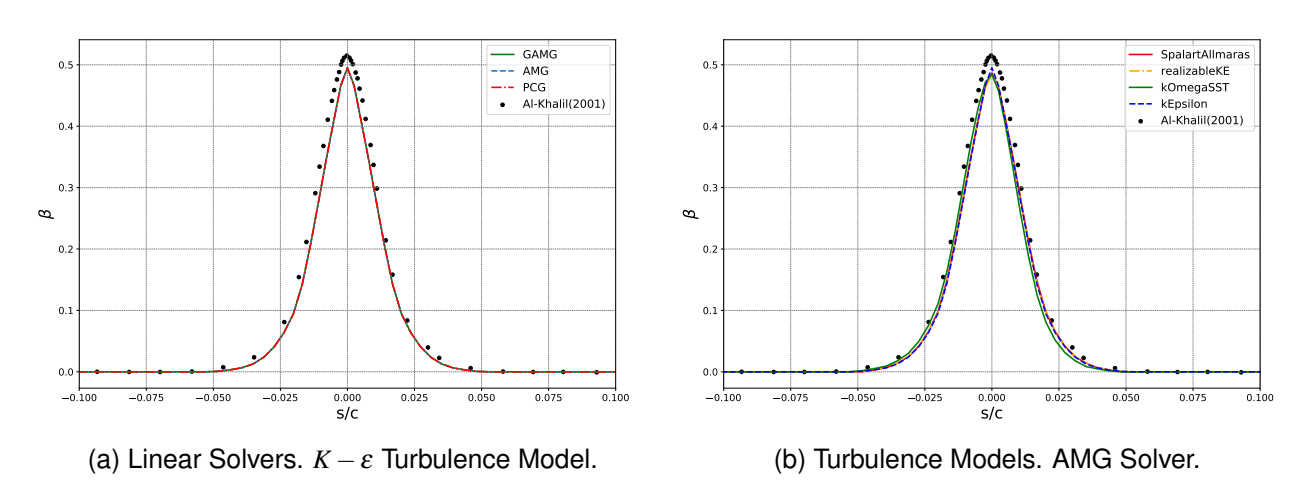


Figure 3 – Langmuir-D [18] - Coarse Mesh.

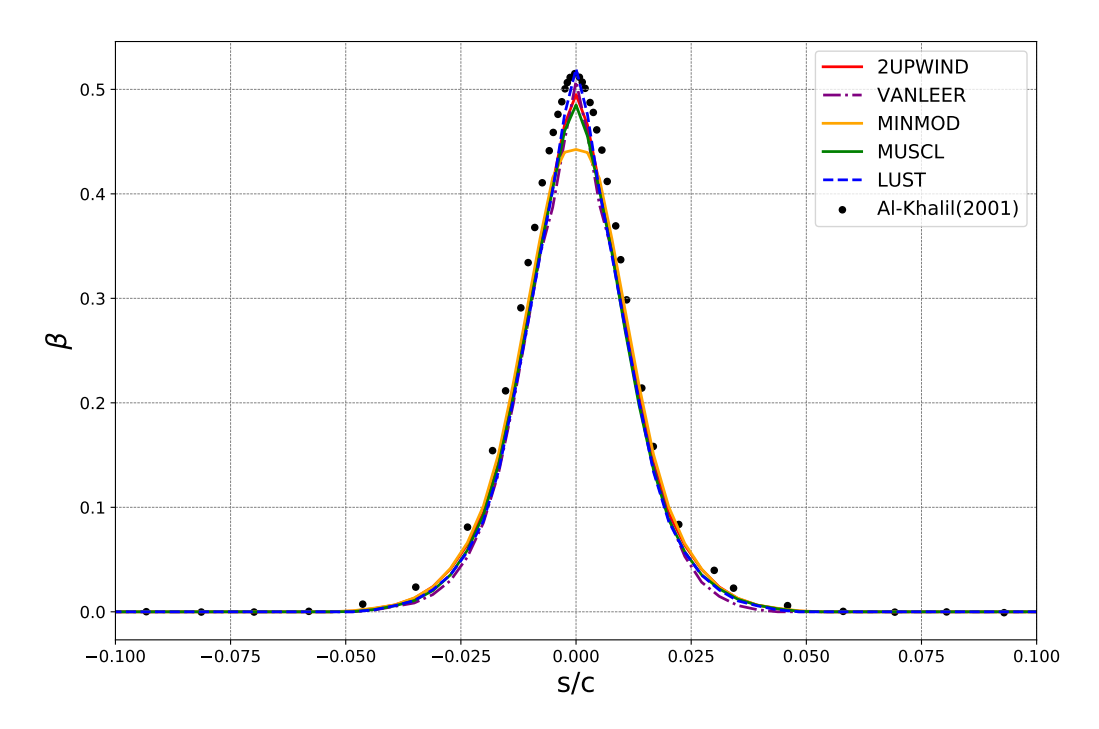


Figure 4 – Langmuir-D [18]. AMG Solver. $K - \varepsilon$ Turbulence Model - Coarse Mesh, TVD Numerical Schemes

7.2 Collection Efficiency - β

The comparison of β values between the linear solvers and Al-Khalil's experimental data is depicted in Figure 3a within the streamwise airfoil region. Preceding the leading edge, the distributions align well with the experimental data. The linear solvers results are very close to each other when you compare the peak, area under the β curve, and average values.

By varying the turbulence models, the results of the numerical distribution of β are compared with Al-Khalil's experimental data in Figure 3b. The growth of the β values in all numerical solutions exhibits a slight delay in comparison to the experimental results (-0.05 < S/C < -0.01) and a premature decrease in the region between 0.02 < S/C < 0.05. In the peak region, see Figure 3b, the $k-\varepsilon$ is the model closest to the correct value.

In Figure 4, a comparison of β distributions involving TVD schemes is presented, including LUST, MUSCL, VANLEER, MINMOD, and Second-Order Upwind. The distributions align well in the region prior to the leading edge. As can be seen in Figure 5, the LUST result shows a close approximation to the experimental result right at the tip of the leading edge, but exhibits lower values for the remaining downstream regions. The Second-Order Upwind closely approximates the experimental data further downstream from peak, but at the peak, it performs worse than LUST yet better than other models. In integral terms, Second-Order Upwind resulted in a close calculation relative to Al-Khalil's β simulations.

Figures 6 and 7 illustrate three simulated droplet distributions: the $20~\mu m$ MVD of Langmuir-D [18], the $20~\mu m$ MVD of Papadakis [17], and the $21~\mu m$ MVD of Wright [16], for coarse and fine mesh, respectively. It is apparent from both plots that the current model employing Langmuir-D in both meshes exhibits a closer alignment with Al-Khalil's LEWICE simulations [5] than the present model utilizing other distributions. This observation suggests that Al-Khalil employed Langmuir-D as the distribution for the simulations. Furthermore, it can be inferred that β calculated with Langmuir-D may not accurately represent the actual NASA icing tunnel, since the experimental distributions of Wright [16] and Papadakis [17] exhibit a larger deviation for β in the region just upstream of the impingement limits compared to the Langmuir-D distribution. Visually, it can be concluded that the simulation with fine mesh produced a β close to the Al-Khalil simulations for all distributions.

The authors also performed a simulation of β for two different meshes, coarse with 7,000 elements

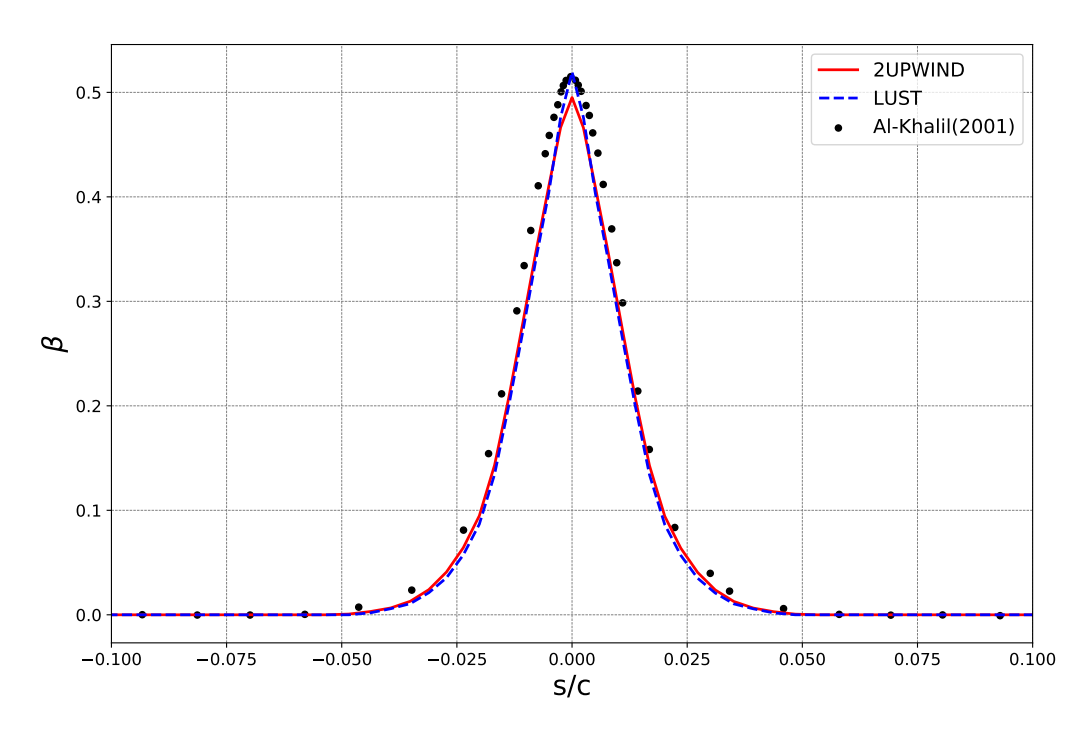


Figure 5 – Langmuir-D [18]. AMG Solver. $K-\varepsilon$ Turbulence Model - Coarse Mesh, TVD LUST vs. Second-Order Upwind

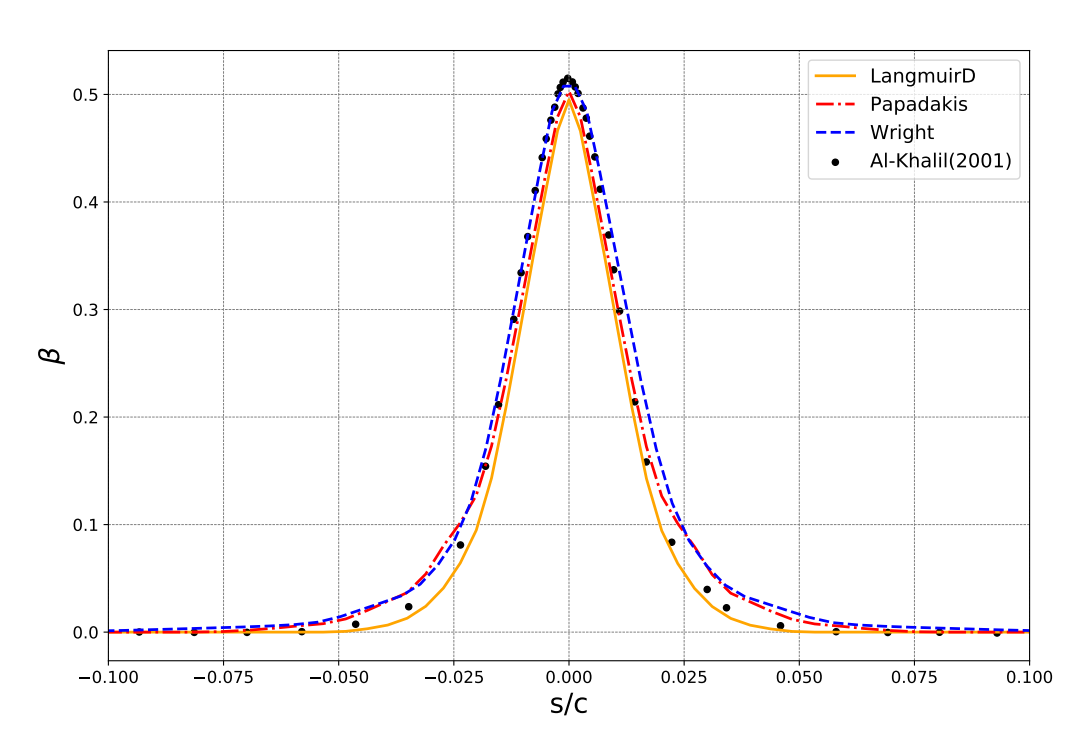


Figure 6 – Langmuir-D [18]. AMG Solver. $K - \varepsilon$ Turbulence Model. TVD Second-Order Upwind - Coarse Mesh.

and fine with 66,000 elements. And also two other droplet size distributions: Wright [16] and Papadakis [17], both based in the Icing Research Tunnel of the Glenn Research Center. Figure 8 shows that the fine mesh has an improved result to replicate the numerical results of Al-Khalil [5] compared to the coarse mesh near the peak and downstream regions. This mesh certainly provides better results with respect to ice accretion and growth, as mentioned before. Nevertheless, the Al-Khalil LEWICE results [5] may not reflect more accurately the actual conditions, as the ice formations

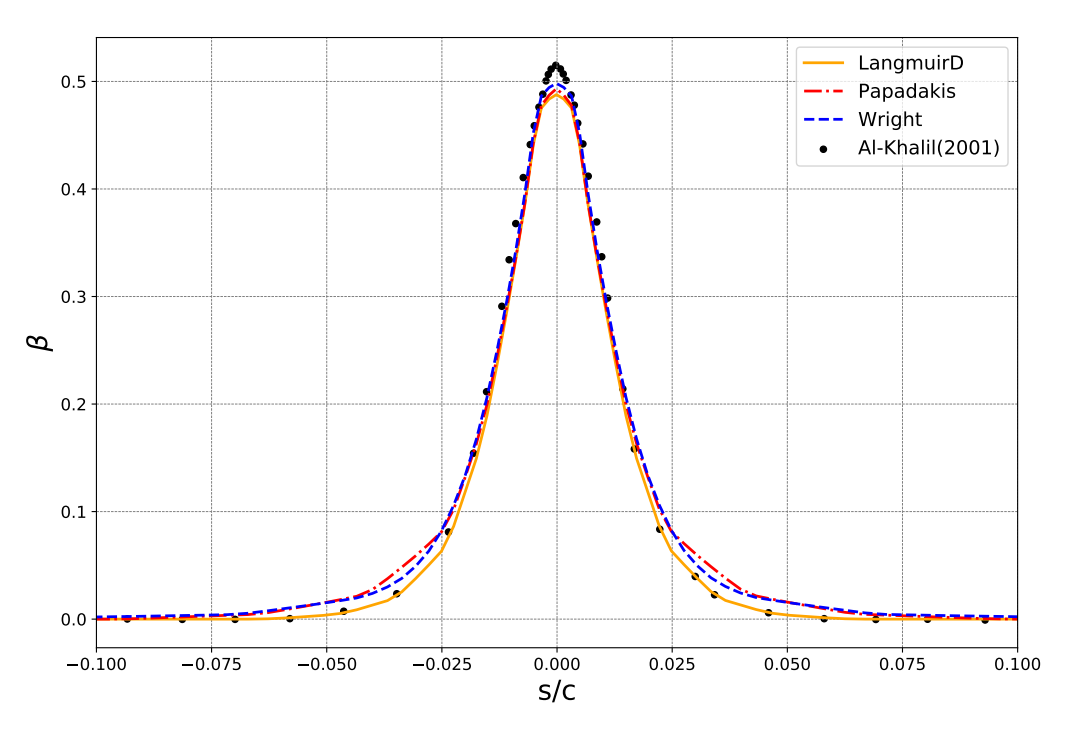


Figure 7 – Langmuir-D [18]. AMG Solver. $K - \varepsilon$ Turbulence Model. TVD Second-Order Upwind - Fine Mesh

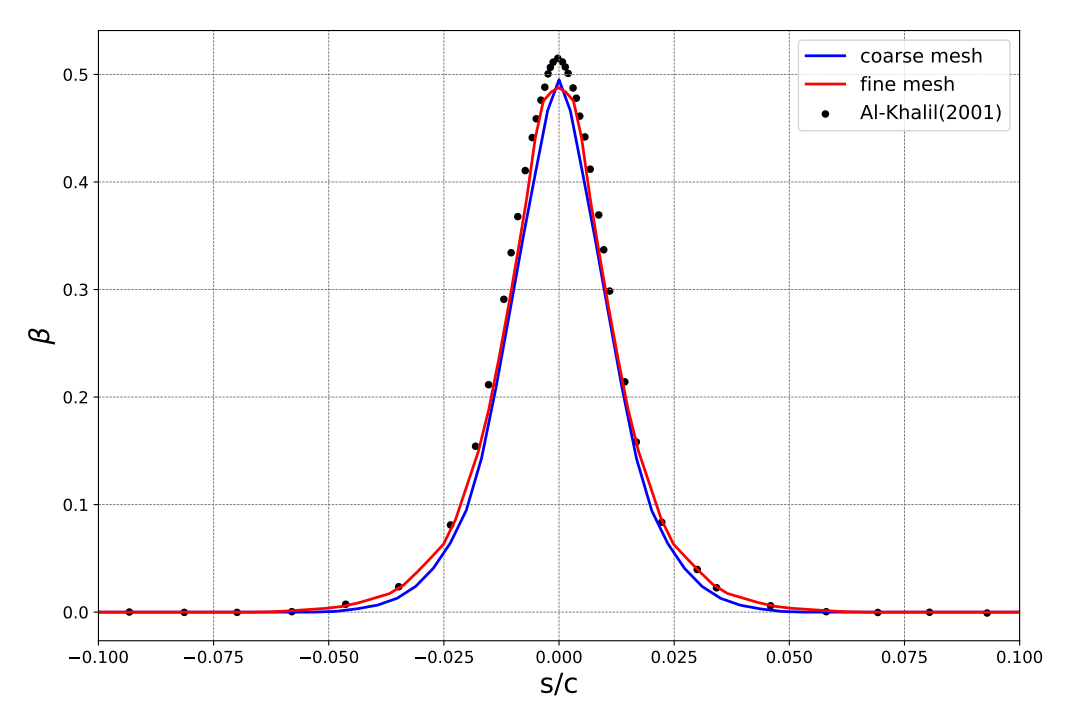


Figure 8 – Langmuir-D [18]. AMG Solver. $K - \varepsilon$ Turbulence Model. TVD Second-Order Upwind - Coarse and Fine Meshes Comparison

predicted by the present model exhibit a closer alignment with the experimental data compared to the LEWICE simulation by Shin and Bond [36]. At stagnation, the reduced values in β do not indicate a diminished ice accretion or a significant deviation in the ice shape at stagnation. Since there is no experimental data available for β in NACA0012 airfoil, it is hard to state that the current model has larger deviations at stagnation. It can also be inferred that the integral under the β curve, representing the quantity of impinged water, likely provides an accurate depiction of the actual scenario, as the

ice shape size predicted by the present model closely align with experimental observations.

7.3 Rime Ice Shapes

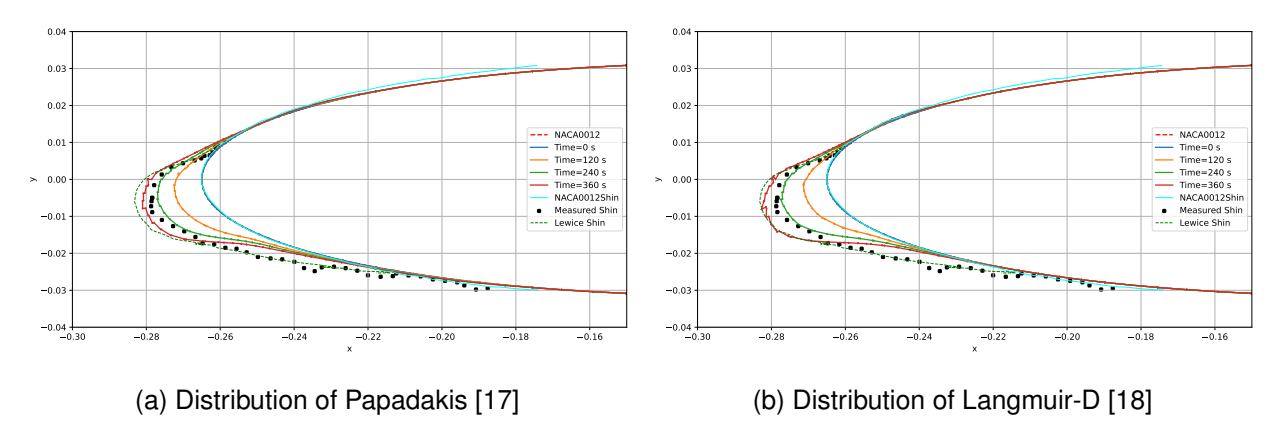


Figure 9 – AMG Solver. $K - \varepsilon$ Turbulence Model. LEWICE ice density model [22]. TVD Second-Order Upwind - Coarse Mesh

After testing C_p and β for several numerical schemes, the rime ice growth simulations used the AMG linear solver for pressure, a $k-\varepsilon$ turbulence model and the Second-Order Upwind TVD scheme. The LUST scheme was also tested to compare the results with the Second-Order Upwind. The duration of the transient flow solution, Unsteady Reynolds Averaged Navier-Stokes (URANS), was set at 1 s, with ice growth occurring over 30 seconds in increments of 12 steps, totaling 360 s of ice accumulation. It is important to note that, despite using the same airfoil, NACA0012, within a subsonic regime of a free-stream Mach number below 0.3, impingement calculations were performed at a zero angle of attack with a chord of 0.9144 m, while the prediction of rime ice accretion was performed at an angle of 4° with a chord of 0.53 m. Furthermore, it should be noted that the parameter β varies with ice accretion at intervals of 30 seconds following an initial 1-second flow solution, in contrast to the impingement calculations, which use a constant β calculated at 2-second flow solution period.

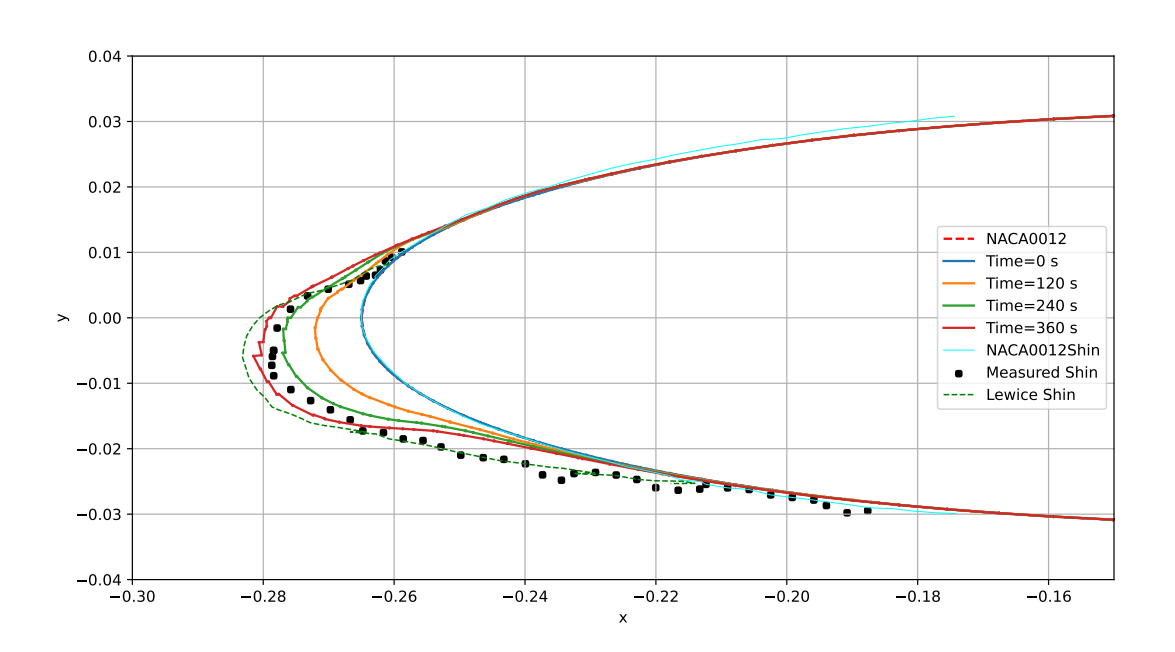


Figure 10 – Distribution of Wright [16]. AMG Solver. $K - \varepsilon$ Turbulence Model. LEWICE ice density model [22] and TVD Second-Order Upwind - Coarse Mesh

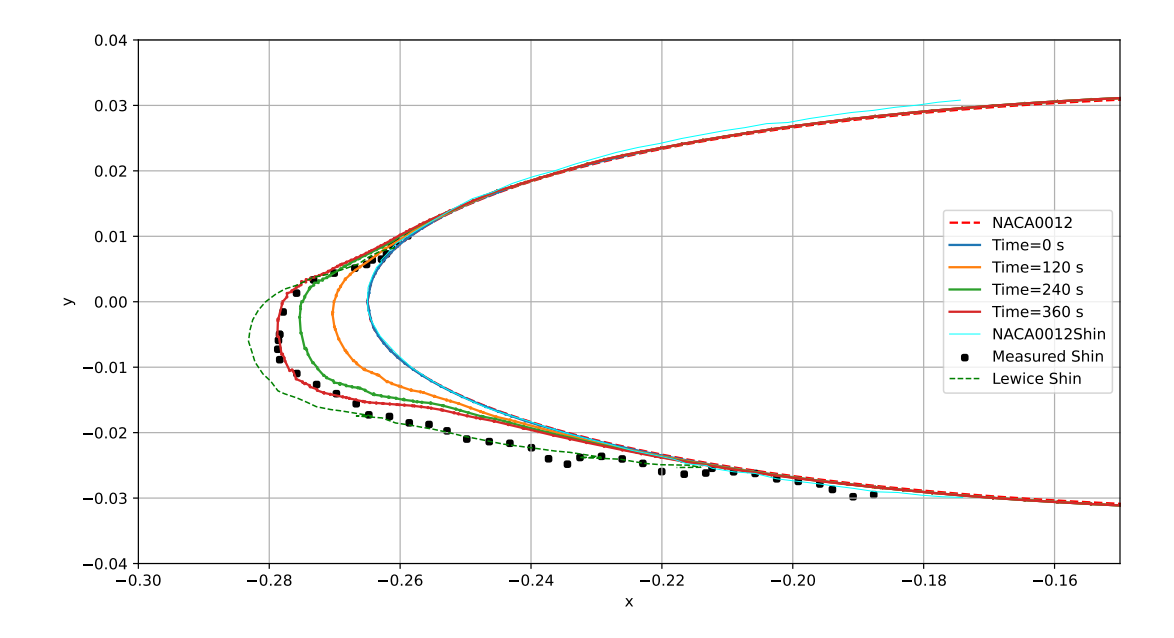


Figure 11 – Distribution of Wright [16]. AMG Solver. $K - \varepsilon$ Turbulence Model. LEWICE ice density model [22] and TVD Second-Order Upwind - Fine Mesh

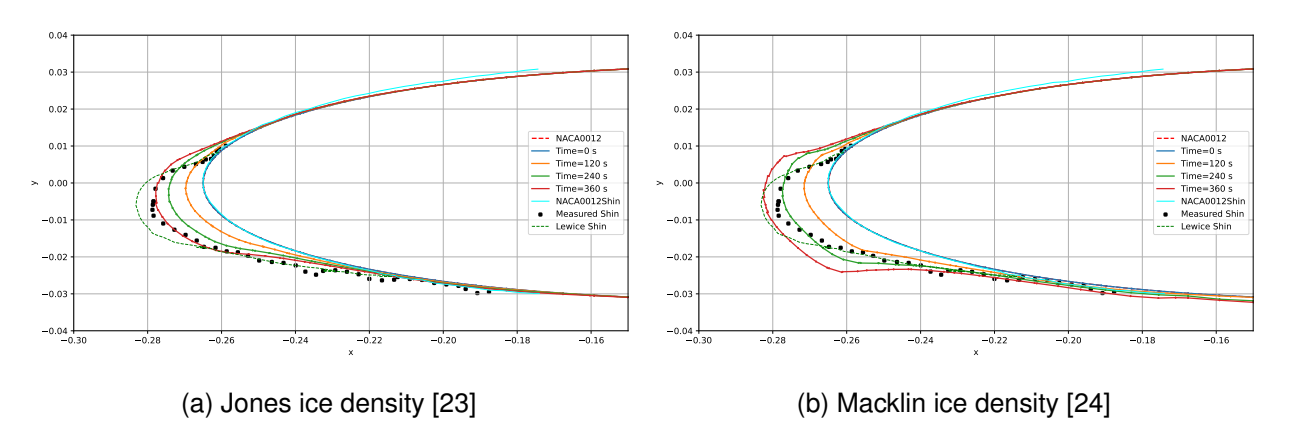


Figure 12 – Distribution of Wright [16]. AMG Solver. $K - \varepsilon$ Turbulence Model. TVD Second-Order Upwind - Coarse Mesh

Three different droplet distribution models were employed: a) theoretical Langmuir-D [18], b) experimental Wright [16], and c) experimental Papadakis [17]. Furthermore, the authors contrasted the ice-shaped resemblance of coarse mesh with those of fine mesh. Lastly, the study highlighted the variations of the TVD Second-Order ice density and TVD LUST, as well as different correlations of the ice density with respect to ice growth and shape.

Using Papadakis' icing tunnel distribution (Figure 9a) with LEWICE ice density, it is possible to see that the overall results tend to match Shin's base case [27, 3]. At the end of the numerical simulation (time = 360 s), it becomes apparent that the numerical results slightly overestimate the shape of the ice, as observed in experiments.

The application of the LEWICE density model along with the Langmuir-D distribution did not successfully replicate the accurate ice shape shown in Figure 10. However, these results were close to the results of the Shin and Bond simulation with LEWICE [27, 3], demonstrating that LEWICE was executed using the Langmuir-D distribution.

Figures 10 and 11 illustrate the shapes of the rime ice computed using the Wright distribution [16], the LEWICE ice density model [22], and the TVD Second-Order Upwind.

In addition, Figure 10 shows the results obtained with a coarse mesh consisting of 7,000 elements,

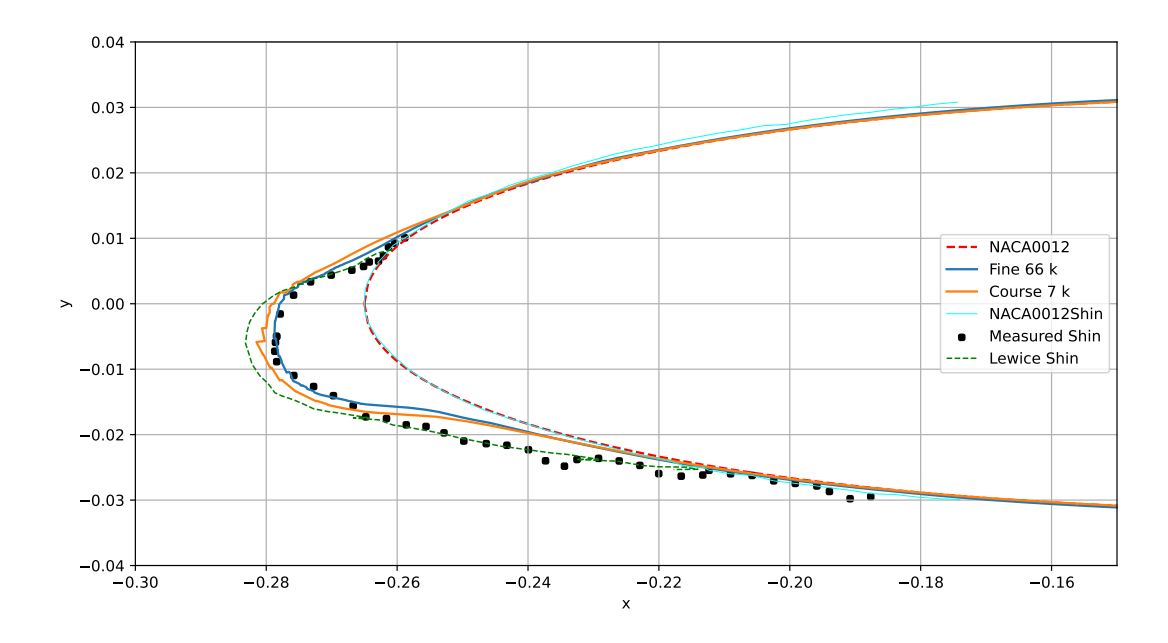


Figure 13 – Distribution of Wright [16]. AMG Solver. $K - \varepsilon$ Turbulence Model. LEWICE ice density model [22] - Fine and Coarse Meshes, TVD Second-Order Upwind

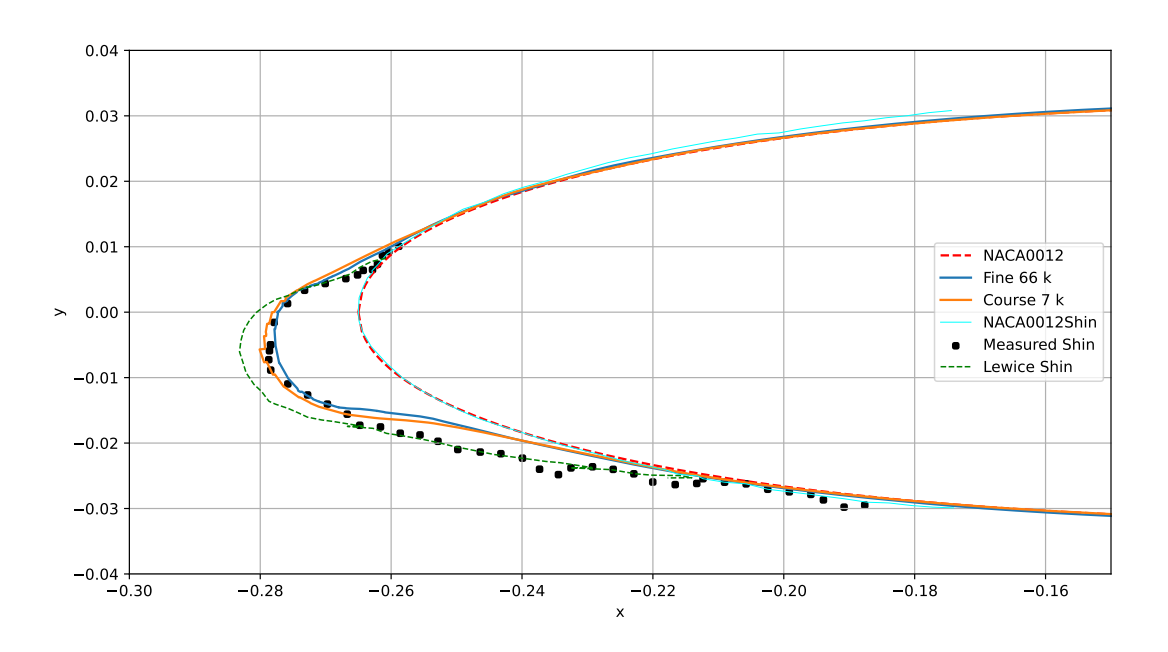


Figure 14 – Distribution of Wright [16]. AMG Solver. $K - \varepsilon$ Turbulence Model. LEWICE ice density model[22] - Fine and Coarse Meshes, TVD LUST

while Figure 11 shows the results obtained with a fine mesh containing 66,000 elements. According to the results obtained using the Wright distribution in Figure 11 with LEWICE ice density, it should be noted that this model exhibited a closer approximation to the ice shape between all tested, making this configuration more suitable for the simulations of the ice shape. However, it also suggests a discrepancy in the lower section, a feature shared by other models. This may point to the presence of a mixed-ice-type scenario, as the current code exclusively computes rime-ice formations. However, the results of the LEWICE code of Shin and Bond [27, 3] show better agreement with the experimental data, particularly in the lower section, than the current model. This is due to the consideration of a wet growth process or mixed ice accretion in LEWICE.

For the results obtained using the Jones density model, there is a greater deviation than the LEWICE model as presented in Figure 12a. However, it is important to note that, in general, the Jones density model exhibited better accuracy than the Macklin ice density model with the same Wright distribution. Furthermore, the results obtained using the Macklin density model in Figure 12b proved to be the least favorable density model among the three models considered.

The influence of the two TVD schemes is shown in Figures 13 and 14. It is apparent that the TVD Second-Order Upwind scheme is slightly better than the LUST scheme on a fine mesh. While the LUST scheme aligns more closely with experimental data than Second-Order Upwind on a coarse mesh, it encounters convergence problems on a fine mesh.

8. Conclusions

This paper has introduced the initial development phase of a 3D ice accretion tool, built on foamextend 5.0. This initial tool is designed to simulate the growth of the rime ice, incorporating features such as a transient flow solution, immersed boundary, Eulerian-dispersed phase modeling, and userdefined droplet distributions.

The authors validated the results of C_p by comparing them with the findings of Emmons [4], assessed β against the research of Al-Khalil et al. [5] numerical simulation with LEWICE, and examined the shape of the rime ice according to a case study by Shin and Bond [3, 27]. The analysis indicated a strong agreement between the simulated results and the experimental data.

The simulation of the present iceAccretionCode for rime ice produced results very close to the experimental data when considering a fine mesh, with 66,000 elements, the Wright [16] distribution, the AMG solver, the $k-\varepsilon$ turbulence model and the LEWICE ice density model [22]. The same configuration produced satisfactory deviations for C_p and β compared to the experimental data and the LEWICE simulations, respectively.

The discrepancies observed in the results for TVD numerical schemes are more pronounced than those arising from variations in the turbulence models and linear solvers for the β simulations. Given that only TVDs significantly impact β and the shape of the rime ice is directly influenced by it, the investigation is confined to the variations in the shape of the ice attributable to different TVDs. This observed invariance with respect to linear solvers and turbulence models may not hold when simulating glaze ice and more complex geometries.

It is essential to acknowledge that the accurate simulation of ice shape is contingent upon the judicious selection of the TVD scheme, a topic frequently overlooked or inadequately addressed in CFD Eulerian simulations. This difference is greater with higher angles of attack than with lower angles due to the increase of the shadow zone formed.

This paper marks the first step towards developing a robust and comprehensive tool for 3D ice accretion simulation, with the ultimate goal of providing an accurate and accepted solution for aviation authorities.

9. Contact Author Email Address

Contact: Guilherme A. Lima da Silva <gasilva@aerothermalsolutions.co>

10. Copyright Statement

The authors confirm that they, and/or their company or organization, hold copyright on all of the original material included in this paper. The authors also confirm that they have obtained permission from the copyright holder of any third party material included in this paper to publish it as part of their paper. The authors confirm that they give permission, or have obtained permission from the copyright holder of this paper, for the publication and distribution of this paper as part of the ICAS proceedings or as individual off-prints from the proceedings.

References

- [1] C. S. Bidwell and M. G. Potapczuk. Users manual for the nasa lewis three-dimensional ice accretion code (lewice 3d). Technical Memorandum NASA TM-105404, NASA, Cleveland, 1993.
- [2] H. Beaugendre, F. Morency, and W. G. Habashi. Fensap-ice's three-dimensional in-flight ice accretion module: Ice3d. *Journal of Aircraft*, 40(2):239, 2003.

- [3] J. Shin and T. H. Bond. Experimental and computational ice shapes and resulting drag increase for a NACA 0012 airfoil. Technical Memorandum TM-105743, National Aeronautics and Space Administration (NASA), Cleveland, 1992. NASA TM-105743. Presented at the 5th Symposium on Numerical and Physical Aspects of Aerodynamic Flows sponsored by California State University Long Beach, California, January 13-16, 1992.
- [4] H. W. Emmons. Flow of a compressible fluid past a symmetrical airfoil in a wind tunnel and in free air. Technical Note NACA TN 1746, National Advisory Committee for Aeronautics, Washington, DC, 1948.
- [5] K. M. Al-Khalil, C. Horvath, D. R. Miller, and W. B. Wright. Validation of nasa thermal ice protection computer codes. part 3: The validation of antice. Technical Memorandum NASA TM-2001-210907, National Aeronautics and Space Administration (NASA), Cleveland, May 2001.
- [6] H. Weller, G. Tabor, H. Jasak, and C. Fureby. A tensorial approach to computational continuum mechanics using object orientated techniques. *Computers in Physics*, 12(6):620–631, 1998.
- [7] H. Jasak, A. Jemcov, and Z. Tukovic. Openfoam: A c++ library for complex physics simulations. In *Coupled Methods in Numerical Dynamics*, Dubrovnik, 2007.
- [8] H. Jasak. Openfoam: Open source cfd in research and industry. In *International Journal of Naval Architecture and Ocean Engineering*, volume 1, pages 89–94, 2009.
- [9] L. M. Stefanini, O. M. Silvares, G. A. L. Silva, and E. J. G. J. Zerbini. Heat transfer on iced cylinders. In *AIAA Paper*, number AIAA-2010-7672, 2010.
- [10] G. A. L. Silva, M. N. Arima, N. N. Branco, and M. M. Pimenta. Proposed wall function models for heat transfer around a cylinder with rough surface in cross flow. In *International Conference on Icing of Aircraft, Engines, and Structures*, number 2011-38-0023, Chicago, 2011.
- [11] L. M. Stefanini, O. M. Silvares, G. A. L. Silva, and E. J. G. J. Zerbini. Convective heat transfer effects in airfoil icing. In *Proceedings of the 19th International Congress of Mechanical Engineering (COBEM 2007)*, number COBEM2007-2222, pages 1–10, 2007.
- [12] L. M. Stefanini. Efeitos da camada limite térmica na formação de gelo em aerofólios de uso aeronáutico. Master's thesis, Escola Politécnica da Universidade de São Paulo, São Paulo, Brazil, 2009.
- [13] Z. Tukovic and H. Jasak. Simulation of free-rising bubble with soluble surfactant using moving mesh finite volume/area method. In *6th International Conference on CFD in Oil & Gas, Metallurgical and Process Industries*, Trondheim, 2008.
- [14] G. A. L. Silva, O. M. Silvares, E. J. G. J. Zerbini, H. Hefazi, H. H. Chen, and K. Kaups. Differential boundary-layer analysis and runback water flow model applied to flow around airfoils with thermal anti-ice. In *AIAA Aerospace Sciences and Meeting*, number 2009-3967, pages 1–12, 2009.
- [15] H. Jasak, D. Rigler, and Ž. Tuković. Design and implementation of immersed boundary method with discrete forcing approach for boundary conditions. In *11th World Congress on Computational Mechanics WCCM XI*, Barcelona, 2014.
- [16] William B. Wright. Validation results for lewice 3.0. NASA Contractor Report NASA/CR-2005-213561, NASA, Cleveland, OH, United States, 2005. Available at NASA Technical Reports Server (NTRS).
- [17] M. Papadakis, M. Breer, N. Craig, and X. Liu. Experimental water droplet impingement data on airfoils, simulated ice shapes, an engine inlet and a finite wing. Contractor Report NASA-CR-4636, NASA, 1994. DOT/FAA/CT-TN93/18, E-9254.
- [18] I. Langmuir and K. Blodgett. In C. Guy Suits and Harold E. Way, editors, *Atmospheric Phenomena*, chapter Mathematical Investigation of Water Droplet Trajectories, pages 335–347. Elsevier. Mathematical Investigation of Water Droplet Trajectories.
- [19] Suhas V Patankar and DB Spalding. A calculation procedure for heat, mass and momentum transfer in three-dimensional parabolic flows. *International journal of heat and mass transfer*, 15(10):1787–1806, 1972.
- [20] Riyad I Issa. Solution of the implicitly discretised fluid flow equations by operator-splitting. *Journal of computational physics*, 62(1):40–65, 1986.
- [21] Hrvoje Jasak. *Error analysis and estimation for the finite volume method with applications to fluid flows.* Ph.d. thesis, Imperial College London, 1996.
- [22] William B. Wright. Update to the nasa lewis ice accretion code lewice. Contractor Report NASA-CR-198355, NYMA, Inc., 1995.
- [23] K. F. Jones. The density of natural ice accretions related to nondimensional icing parameters. *Quarterly Journal of the Royal Meteorological Society*, 116(492):477–496, 1990.
- [24] W. C. Macklin. The density and structure of ice formed by accretion. *Quarterly Journal of the Royal Meteorological Society*, 88(375):30–50, 1962.
- [25] Federal Aviation Administration. Aircraft Ice Protection. Federal Aviation Administration, Dec 2007. FAA

- AC 20-73A. Accessed on July 4, 2024.
- [26] Mark Drela. Xfoil: An analysis and design system for low reynolds number airfoils. In Thomas J. Mueller, editor, Low Reynolds Number Aerodynamics, volume 54 of Lecture Notes in Engineering. Springer, Berlin, Heidelberg, 1989.
- [27] Jaiwon Shin and Thomas H. Bond. Results of an icing test on a naca 0012 airfoil in the nasa lewis icing. In 30th Aerospace Sciences Meeting and Exhibit, number AIAA-92-0647. American Institute of Aeronautics and Astronautics, 1992.
- [28] Magnus R. Hestenes and Eduard Stiefel. Methods of conjugate gradients for solving linear systems. Journal of Research of the National Bureau of Standards, 49:409–436, 1952.
- [29] John Ruge and Klaus Stüben. Algebraic multigrid (amg). Multigrid Methods, 3:73-130, 1987.
- [30] Klaus Stüben. A review of algebraic multigrid. *Journal of Computational and Applied Mathematics*, 128:281–309, 1999.
- [31] D. B. Spalding. A novel finite difference formulation for differential expressions involving both first and second derivatives. *International Journal for Numerical Methods in Engineering*, 4:551–559, 1972.
- [32] Bram Van Leer. Towards the ultimate conservative difference scheme v. a second order sequel to godunov's method. *Journal of Computational Physics*, 32:101–136, 1979.
- [33] Bram Van Leer. Flux-vector splitting for the euler equations. *Lecture Notes in Physics*, 170:507–512, 1982.
- [34] P. L. Roe. Characteristic-based schemes for the euler equations. *Annual Review of Fluid Mechanics*, 18:337–365, 1986.
- [35] B. P. Leonard. The ultimate conservative difference scheme applied to unsteady one-dimensional advection. Computer Methods in Applied Mechanics and Engineering, 88:17–74, 1991.
- [36] Tsan-Hsing Shih, William W. Liou, Aamir Shabbir, Zhu Yang, and J. Zhu. A new $k \varepsilon$ eddy viscosity model for high reynolds number turbulent flows. *Computers & Fluids*, 24(3):227–238, 1995.
- [37] Florian R. Menter. Two-equation eddy-viscosity turbulence models for engineering applications. *AIAA Journal*, 32(8):1598–1605, 1994.
- [38] Philippe R. Spalart and Steven R. Allmaras. A one-equation turbulence model for aerodynamic flows. *La Recherche Aerospatiale*, pages 5–21, 1992.
- [39] W. P. Jones and B. E. Launder. Predictions of some common aerodynamic flows with a two-equation model of turbulence. *International Journal of Heat and Mass Transfer*, 15:301–314, 1972.
- [40] Theodore von Karman and Hsue-shen Tsien. The fundamental principles of flow in the boundary layer in compressible fluids. *Journal of the Aeronautical Sciences*, 5(10):227–240, 1938.
- [41] Hermann Glauert. Approximate calculation of the lift of an airfoil in a compressible flow. Technical report, NACA TM-562, 1928. Translated from "Die Gesetze des Luftwiderstandes," ZFM, Vol. 4, No. 1, 1923.